Citation for published version:
Kimber, RGE, Wright, EN, O'Kane, SEJ, Walker, AB & Blakesley, JC 2012, 'Mesoscopic kinetic Monte Carlo modeling of organic photovoltaic device characteristics', Physical Review B, vol. 86, no. 23, 235206. https://doi.org/10.1103/PhysRevB.86.235206

DOI:
10.1103/PhysRevB.86.235206

Publication date:
2012

Document Version
Publisher's PDF, also known as Version of record

Kimber, R.G.E.; Wright, E.N.; O'Kane, S.E.J.; Walker, A.B.; Blakesley, J.C. / Mesoscopic kinetic Monte Carlo modeling of organic photovoltaic device characteristics.
In: Physical Review B, Vol. 86, No. 23, 26.12.2012, art. no. 235206.

PHYSICAL REVIEW B **86**, 235206 (2012)

Mesoscopic kinetic Monte Carlo modeling of organic photovoltaic device characteristics

Robin G. E. Kimber, Edward N. Wright, Simon E. J. O'Kane,[*] and Alison B. Walker[†]
Department of Physics, University of Bath, Bath BA2 7AY, United Kingdom

James C. Blakesley
Institut für Physik und Astronomie, Universität Potsdam, Physik weicher Materie, Karl-Liebknecht-Strasse 24-25, 14476 Potsdam-Golm, Germany

(Received 5 April 2012; revised manuscript received 10 September 2012; published 26 December 2012)

Measured mobility and current-voltage characteristics of single layer and photovoltaic (PV) devices composed of poly{9,9-dioctylfluorene-co-bis[N,N'-(4-butylphenyl)]bis(N,N'-phenyl-1,4-phenylene)diamine} (PFB) and poly(9,9-dioctylfluorene-co-benzothiadiazole) (F8BT) have been reproduced by a mesoscopic model employing the kinetic Monte Carlo (KMC) approach. Our aim is to show how to avoid the uncertainties common in electrical transport models arising from the need to fit a large number of parameters when little information is available, for example, a single current-voltage curve. Here, simulation parameters are derived from a series of measurements using a self-consistent "building-blocks" approach, starting from data on the simplest systems. We found that site energies show disorder and that correlations in the site energies and a distribution of deep traps must be included in order to reproduce measured charge mobility-field curves at low charge densities in bulk PFB and F8BT. The parameter set from the mobility-field curves reproduces the unipolar current in single layers of PFB and F8BT and allows us to deduce charge injection barriers. Finally, by combining these disorder descriptions and injection barriers with an optical model, the external quantum efficiency and current densities of blend and bilayer organic PV devices can be successfully reproduced across a voltage range encompassing reverse and forward bias, with the recombination rate the only parameter to be fitted, found to be 1×10^7 s^{-1}. These findings demonstrate an approach that removes some of the arbitrariness present in transport models of organic devices, which validates the KMC as an accurate description of organic optoelectronic systems, and provides information on the microscopic origins of the device behavior.

DOI: 10.1103/PhysRevB.86.235206 PACS number(s): 73.50.Pz, 72.80.Le, 81.05.Lg

I. INTRODUCTION

Optoelectronic devices consisting of organic semiconductors, such as organic field effect transistors (OFETs), organic photovoltaics (OPVs), and organic light-emitting displays (OLEDs), are attracting a lot of research interest as they have the potential to make cheap and easy-to-produce alternatives to inorganic devices. However, organic semiconductors typically have low mobilities $\sim$0.1 cm^2 V^{-1} s^{-1} compared to their inorganic counterparts $\sim$10 cm^2 V^{-1} s^{-1}, which currently limits their use for practical electronics, for example, low charge mobilities result in a slow response time in OFETs and reduced power conversion efficiencies in OPVs. Organic devices also suffer from internal degradation caused by the movement of charge and energy about the organic semiconductors. In OPVs, charge separation and recombination occur at the interface of the donor and acceptor components and are sensitive to the distribution of acceptor and donor molecules. Consequently, in all organic devices, the performance of the device will depend strongly on the chemical structure and morphology, the latter determined by the fabrication of the device. As new materials are synthesized, it is helpful to have a strategy for finding simulation parameters that gives values that are determined by the material alone (plus the contact where injection barriers are concerned) and are transferable between device configurations.

In the organic polymers that are the focus of this paper, charge carriers couple to phonons to become polarons localized to conjugated segments, regions of the chains of a few monomers in extent. Transport occurs through polaron hopping between these states, which have a distribution of energies. In the last few years, many groups, for example,[1–8] have shown that charge transport in polymers can only be understood by invoking deep traps, that is, charge states whose energies lie too deep in the band gap in concentrations too great to be accounted by tail states in the energetic distribution.

References 1–8 have employed drift-diffusion models in which the coupled drift and diffusion equations that describe charge transport are solved. These models assume the semiconductor to be homogeneous and so solve the equations in one dimension along a direction normal to the electrodes. However, in OPVs the charges are confined to separate phases and are generated and recombine at the interface between these phases. Drift-diffusion models have been solved for two phase systems in a two-dimensional interdigitated morphology[9,10] but these papers could not take full account of the effect of three-dimensional structures on the key processes of charge transport, recombination. Exciton dissociation takes place via several intermediate steps,[9] which are critically influenced by morphology.[11,12] Three-dimensional modeling can be achieved by solving the Pauli master equation for the occupation probabilities of the sites on a lattice, based on hopping rates between sites, from which currents can be calculated.[13,14] This approach has provided much insight into OPVs but is limited to low charge densities and steady-state solutions.[13,15]

KMC is a dynamical model designed to account for several species of interacting particles with many possible reactions that take place over a wide range of time scales in three dimensions (3D), first introduced for OPVs by Watkins *et al.*[16] and explored further by us in Refs. 17 and 18. Its methodology has been assessed in Ref. 19 and it has been used to study how morphology influences device performance, for example, interface structure.[20] Here, we use the KMC to model a group of transport characteristics using a self-consistent "building blocks" approach in order to derive and use simulation parameters with minimal adjustment.

Our model is similar to previous work by the authors,[16,17] but we have improved our description charge injection and hence forward bias currents. Given the density-dependence of the mobility, the independent carrier assumption[21,22] when modeling injection and subsequent current flow is invalid for the present work.[13] The zero-field, zero-carrier density mobility μ_0, the energetic distribution width σ for the two polymers, and correlation length ξ for the energies agree well with values deduced from a drift-diffusion model[23] derived for the zero carrier density (i.e., single particle) case.

We find it necessary to include correlations in the site energies and an exponential distribution of deep traps to fit the data of Ref. 23, a conclusion also reached by Refs. 1–8,24. These parameters are then used to reproduce measured single-layer, unipolar current density J vs applied bias V characteristics. At this stage the injection barriers for electrons and holes are the only unknown parameters and can therefore be deduced from fitting predicted to measured J-V curves.

Finally, these parameters were combined with an optical model to reproduce the complete J-V and external quantum efficiency (EQE) characteristics of bilayer and blend devices with the geometries shown in Fig. 1 across a range of biases by fitting the exciton dissociation rate. In this way we avoid the difficulties ensuing from fitting many unknown simulation parameters to a limited amount of data.

The layout of this paper is as follows: Section II describes our model, Sec. III presents the results, and Sec. IV concludes.

II. MODEL

We have represented carrier motion by thermally assisted hopping between sites on a 3D Cartesian lattice of lattice constant $a = 1$ nm. Three species of particles are considered: electrons, holes, and excitons. Multiple occupation of polymer sites by any species is forbidden unless at electrode sites. In this way Zhou *et al.*[25] have shown that carrier concentration dependence, given by a density-dependent factor in the mobilities in references,[26–29] is well represented in KMC.

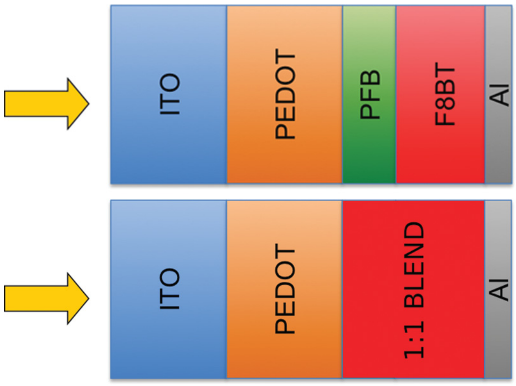

FIG. 1. (Color online) Schematic diagrams showing (a) bilayer device and (b) blend device geometries. The arrow shows the direction of illumination. Layer thicknesses are specified in Table I.

Periodic boundary conditions are applied in the y and z dimensions, and for mobility-only simulations, are applied in all three dimensions to allow for continuous charge transport. Devices of dimensions (L_X, L_Y, L_Z) were modeled, where electrodes are at $x = 0$ and $x = L_X$, where L_X denotes the length of the device and the electrodes are parallel to the (y,z) plane. $L_Y = L_Z = 50$ nm, a sufficient length to eliminate finite-size effects. The lattice sites in the bulk of the simulation are denoted as either electron-transporting sites, n, or hole-transporting sites, p, with carriers confined to their respective mediums. Excitons in the bulk are free to roam all sites, but will always dissociate if they encounter a heterojunction between n- and p-type sites.

Electrons and holes can recombine across the heterojunction at a rate k_r. For the blend, how sites are chosen to be n or p for a given interfacial area, or equivalently domain size, is described in Refs. 16 and 17. The n- and p-type domain sizes within the blend in the measured devices were not known, except that a typical domain size is less than 10 nm, so the domain size used in the simulation was 1.4 nm.

The simulation proceeds by executing a chronological series of events, also termed reactions, encompassing all of the particles contained within the simulated system. In contrast to the first reaction method (FRM), often employed for OPV simulations,[16,30] we have recalculated every event at every time step in the simulation. This procedure ensures accuracy at forward bias, where current densities are higher than those encountered under normal photovoltaic operating conditions. Further details of the FRM and its contrast with the simulation methodology utilized here can be found in Ref. 18.

For each particle in the system, the next reaction has a rate, k, associated with it. This rate depends on the type of reaction involved (hop, extraction, recombination, etc.), and the energy difference between the sites involved (if more than one site is involved). The subsequent waiting time, t_i, for the ith reaction is calculated via inverse transform sampling,[31]

$$t_i = -\frac{\ln(R_i)}{k}, \tag{1}$$

where R_i is a uniformly distributed random number between 0 and 1. The next reaction, and its associated waiting time, is calculated for every particle in the system. The event with the shortest waiting time is then executed, resulting in the system evolving to another state, at which point the simulation time is incremented by the waiting time of the executed event. New events are then found for the particle(s) involved in the reaction, as well as all others in the system, due to the changes induced by the previous reaction. Again, the event with the shortest waiting time is executed, and the process is then repeated until the system has reached a steady state for long enough to produce consistent results.

Energetic disorder within the device arising from variations in conjugated segment lengths is simulated by the Gaussian disorder model (GDM),[21] where the contribution to the energy of the hopping site i, $E_{i\mathrm{GDM}}$, is taken from a Gaussian distribution of width σ. Simulations were performed across the range $\sigma = 60$ to 160 meV.

Spatial correlation has been observed in some materials, and as well as better reproducing the field dependence of the mobility, can also be used to account for the level of charge trapping at heterojunctions and hence geminate pair behavior.[32] The origin of the energetic correlations has been attributed to various causes, such as the interaction of carriers with an ensemble of randomly oriented electric dipoles, or to thermal fluctuations of the molecular geometry, combined with steric restoring forces.[33] Here we have implemented the method developed by Gartstein *et al.*[34] to find the energy E_i of site i starting from the GDM by

$$E_{\sigma i} = \frac{1}{\sqrt{n}} \Sigma_{i=1}^{n} E_{i\mathrm{GDM}}, \tag{2}$$

where n is the number of sites a distance ξ from site i and $\xi \sim$ hopping site size a.[7,35,36] This method produces short-range correlations with an inverse distance decay that retain an overall Gaussian distribution of site energies with the same width σ used in the GDM.

The density of deep trap states over trap energies E to $E + \mathrm{d}E$ takes a widely adopted form, for example,[5]

$$f(E)\mathrm{d}E = \frac{\mathrm{d}E}{k_B T_0} \exp\left(\frac{E}{k_B T_0}\right), \tag{3}$$

where T_0 is the characteristic temperature of the trap distribution. Energies sampled from this density of states were generated using an inverse transform sampling method, analogous to that described above for event waiting times.

The energy of the ith site for an electron at a distance x_i from the cathode can be expressed as

$$E_i = \phi_W + \phi_B + E_{\sigma i} - eFx_i + e\Delta V - \frac{e^2}{16\pi\epsilon_0\epsilon_r x_i}, \tag{4}$$

where ϕ_W is the electrode work function, ϕ_B is the injection barrier for electrons, F is the net field resulting from the applied bias and the built-in voltage, V_{bi}, and the last term accounts for image charge effects. An equivalent expression for E_i exists for hole transport. Electrostatic contributions to E_i from other charges in the system are accounted for by

$$\Delta V = \sum_{j=1}^{N-1} \frac{qe}{4\pi\epsilon_0\epsilon_r r_{ij}}. \tag{5}$$

Here N is the number of charges in the device; $q = +e$ for electron-electron and hole-hole repulsion and $-e$ for electron-hole attraction and ϵ_r is the dielectric constant of the polymer which has been set at 3.5, a typical value for organic semiconductors.[23]

In other KMC models,[16,30,37] whenever a charge moved, ΔV has been calculated for every site within a specified cutoff radius, r_c, of the old and new locations of the charge, and the electron and hole arrays updated. However, this approach is unnecessarily computationally intensive for the charge densities simulated in this work. Instead, when determining the waiting time for a charge hopping event, ΔV is only calculated for the current location of the charge and for each possible destination site, reducing the computing resource required and extending the range of influence of each charge to the entire system. Due to the low charge densities in OPVs, the contributions to ΔV from other carriers' mirror charges are not included since Refs. 13 and 38 showed that multiple electrode reflections of the image charge can be ignored for potentials $r_c > 16$ nm.

The rate associated for a charge hopping in the bulk from site i to site j is governed by Marcus theory,[39]

$$k_{ij} = \nu_{\mathrm{hop}} \exp[-2\alpha r_{ij}] \exp\left[-\frac{(E_j - E_i + \lambda)^2}{4\lambda k_B T}\right], \tag{6}$$

where ν_{hop} is the hopping prefactor, calculated with reference to the Einstein-Smoluchowski relation;[40,41] α represents the charge localization constant, set as 2 nm^{-1} (Ref. 16); r_{ij} is the distance between sites i and j; λ corresponds to the reorganization energy cost in transporting the charge from one conjugated segment to the next (represented by lattice sites i and j), here set equal to 0.75 eV (Ref. 12); and E_i and E_j are the energies associated with the ith and jth sites, respectively. For charge transport in the bulk, Marcus theory has been utilized as it can be linked to parameters derived either from experiment or atomistic modeling[42] and has been used in multiscale models of charge transport.[15,42,43] However, the Marcus rate is not applicable to the process of charge injection from electrode sites into the bulk, so this process is described using the conventional Miller-Abrahams rate equation,[44,45]

$$k_{ij} = \hat{\nu}_{\mathrm{hop}} \exp[-2\alpha r_{ij}] f(E_i, E_j), \tag{7}$$

where $f(E_i, E_j)$ is the Boltzmann factor, utilized to maintain detailed balance,

$$f(E_i, E_j) = \begin{cases} \exp\left[-\frac{E_j - E_i}{k_B T}\right] & E_j > E_i, \\ 1 & E_j < E_i. \end{cases} \tag{8}$$

Here, $\hat{\nu}_{\mathrm{hop}}$ is the hopping prefactor for injection.

We follow the procedure established by Gartstein *et al.*[34] to find the mobility in a contactless simulation at a constant field F. A charge is assigned a random location within the device as a starting point. We continue the simulation of each trajectory until the net displacement of the charge parallel to the field reaches a predefined value, d. This approach allows a charge to sample available energy states even when encountering a deep trap that may cause the trap to visit the trap site many times. The time t taken for the random walk determines the mobility through $\mu = d/(tF)$. The simulation is then reset for a new charge, and the mobility is averaged over 100 charges × 500 reconfigurations of the same disorder parameters. We have confirmed that our method gives the same results as simulations in which a fixed number of hops is used, noting that for such simulations, the large number of hops needed to ensure adequate sampling of the energetic landscape leads to very large demands on computer resources.

To remove as far as possible all adjustable parameters from the simulation we use an optical model to calculate the distribution of absorbed photons. The optical model determines the internal optical field, $E(x)$, from which the time average of the energy dissipated per second at a depth x within the device, $Q(x)$, determining the distribution of resultant excitons can be found,[46]

$$Q(x) = \tfrac{1}{2} c\epsilon_0 \alpha\eta E^2, \tag{9}$$

TABLE I. Optical constants employed in the bilayer and blend PV devices.

	Width (nm)	η	κ	Reference
Glass		1.5	0	47
ITO	120	1.9	3.8×10^{-3}	46,47
PEDOT	120	1.5	2.5×10^{-2}	46,47
PFB (bilayer)	45	1.8	1.2×10^{-2}	48
F8BT (bilayer)	90	1.7	6.4×10^{-1}	48
PFB/F8BT (blend)	100	1.8	3.3×10^{-1}	48
Al	150	0.6	5.2	48

where c is the speed of light, ϵ_0 the vacuum permittivity, and the attenuation coefficient α is obtained from the extinction coefficient κ by $\alpha = 4\pi\kappa/\lambda$. The complex refractive index is $\tilde{n} = \eta + i\kappa$. All the experimental work was performed with a monochromatic light source of wavelength $\lambda = 460$ nm. Optical values used here are given in Table I. These values have been calculated from the experimental data in Ref. 23, where possible; otherwise, they are from the cited references.

An optical model to predict the bilayer and blend PV devices shown schematically in Fig. 1 has been undertaken. This model accounts for reflection of light at each interface. The optical electric fields, $|E(x)|$, and absorption distributions, $Q(x)$, for these devices, normalized to their peak value, are shown in Figs. 2 and 3, respectively. These quantities have been calculated for $\lambda = 460$ nm, using the values given in Table I. For the PFB/F8BT blend, the mean of the values for PFB and F8BT was used as the composition ratio of the two polymers was not known and the values are sufficiently close that a more exact approach was not justified.

A random number, R, between 0 and 1 is generated. If $R < Q(x)/Q_{\max}$, where $Q_{\max}$ is the maximum value of $Q(x)$ across the device, the location is chosen as the site for the generation of an exciton. If not, the process is repeated with new sites until one is accepted. Subsequent exciton diffusion is simulated using the Förster energy-transfer rate for excitons,[49]

$$k_{ij} = \frac{1}{\tau}\left[\frac{r_f}{r_{ij}}\right]^6 f(E_i, E_j), \tag{10}$$

where τ is the exciton lifetime and r_f is the Förster radius. The energy landscape that the excitons explore depends only on the disorder term $E_{\sigma i}$, due to their charge-neutral behavior. To avoid making the exciton diffusion length an adjustable simulation parameter, it has been assumed that the energetic distribution of chromophores is identical to $E_{i\mathrm{GDM}}$, and the values for $\tau = 500$ ps and $r_f = 3.1$ nm are taken from Ref. 49.

In the KMC simulations, the EQE is determined from $\eta_a\eta_{ed}\eta_{cc}$, where η_a is the absorbed fraction of the incident photon flux, η_{ed} the exciton dissociation efficiency, that is, the proportion of photogenerated excitons which successfully dissociate into charge pairs, and η_{cc} the charge collection efficiency, that is, the fraction of charge pairs that are successfully extracted at the electrodes. Our predicted EQE is compared with the measured EQE, obtained from the illuminated and dark current densities J_{Total} and J_{Dark}, respectively, and the incident light power density M by $(J_{\mathrm{Total}} - J_{\mathrm{Dark}})/M$.

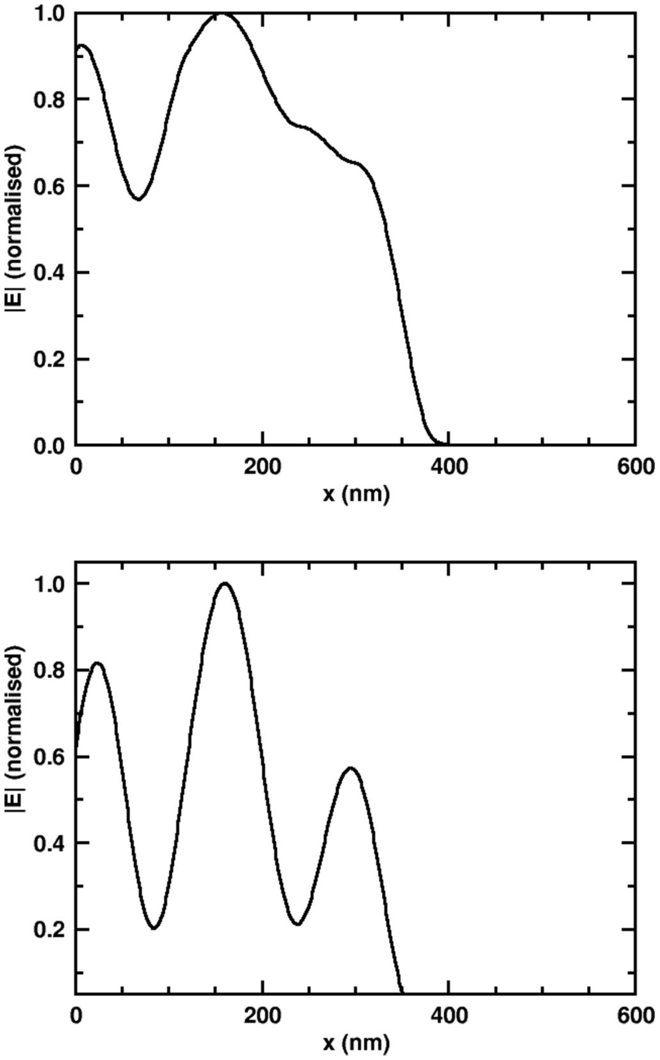

FIG. 2. Magnitude of field $E(x)$ from optical illumination normalized to its peak value. (Top) Bilayer device; (bottom) blend device.

III. RESULTS AND DISCUSSION

Figure 4 shows our predicted PFB mobility-field characteristics for different energetic landscapes for the field range used in Ref. 23, namely $F^{0.5} = 10^3$ to 10^4 $(\mathrm{V/m})^{0.5}$. The Poole-Frenkel (PF) field dependence for the carrier mobility, μ, widely observed in organic semiconducting devices,[13,23,40,50] is given by the expression

$$\mu(F) = \mu_0 \exp(\gamma\sqrt{F}), \tag{11}$$

where μ_0 is the zero-field mobility and γ is a measure of the strength of the field dependence. We kept σ fixed at 115 meV, close to the value obtained by Ref. 23, shown in Table II that also shows μ_0 and γ for PFB and F8BT. These values were obtained at zero carrier density by including the mobility variation in Eq. (11) in a drift-diffusion model that allows for variation of the mobility with charge density using the GDM and fitting the predicted current-voltage curves to experimental measurements for a wide range of device temperatures and thicknesses.[23]

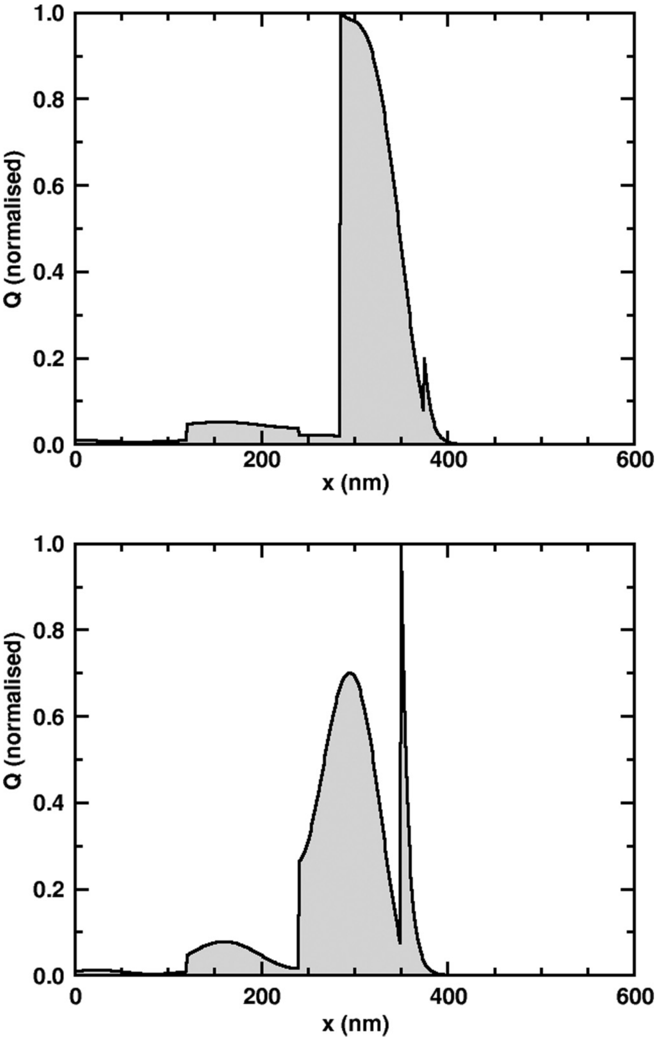

FIG. 3. Time averaged rate of energy dissipation $Q(x)$ from optical field normalized to its peak value. Top panel: bilayer device, bottom panel: blend device.

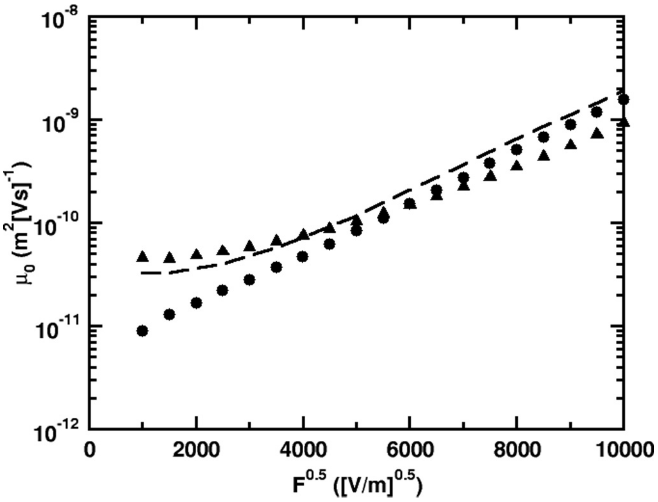

FIG. 4. PFB mobility vs field F $\mu(F)$. Site energies taken from GDM (△), where disorder width $\sigma = 115$ meV; CDM (dashed line), where correlation range $\xi = 2$ nm; and CDM with traps (●), where percentage of trap sites $\varphi = 0.3\%$ and trap distribution width $T_0 = 1225$ K. The CDM with traps reproduces the experimental PF dependence down to the lowest field in the range measured with $\gamma = 7.7 \times 10^{-4}$ m$^{0.5}$ V$^{-0.5}$, $\mu_0 = 2 \times 10^{-13}$ m^2/(Vs).

From Fig. 4, the GDM alone is insufficient for reproducing the PF field dependence, suggesting the energetic landscape to be more complex. Correlating the site energies using the CDM [Eq. (2)] increases the field range over which PF behavior is observed, with PF field dependence seen over the widest range of fields if $\xi = 2$ nm. The sensitivity of the mobility field curves to ξ is further discussed in Ref. 51, where extensive preliminary simulations were reported that tested a range of correlation lengths, with the result that $\xi = 2$ nm gave the best fit to the PF dependence. Reference 23 stated that some form of correlated disorder is necessary to fully explain the field dependence in agreement with Fig. 4. Even with correlations, there is a breakdown of PF dependence at low field and traps with the distribution of Eq. (3) and the parameter values shown in the figure caption must be introduced. Other trapping distributions of $(\varphi, T_0) = 0.1\%$, 1600 K; 0.3%, 1225 K; and 0.9%, 1050 K produced identical results. In Ref. 23, a trap distribution was not included, but the similarity between the value of σ deduced for F8BT (100 ± 10 meV) and the characteristic energy of the trap-only distribution deduced by Steyrleuthner (≈100 meV) for the same polymer[5] was noted since this similarity suggests similar underlying physics between the two models.

Figures 5(a) and 5(b) indicate the sensitivity of μ_0 and γ to the characteristic trapping temperature T_0 and the percentage of trap sites φ. Figures 6(a) and 6(b) show how PF dependence breaks down at low fields for different trap distributions.

For F8BT, although a reasonable fit can be found while remaining within the range of σ specified in Ref. 23, the quality of fit was lower than was achieved for PFB. An excellent fit to the benchmark values was achieved for $\sigma =$ 160 meV, $\xi = 2$ nm, $\varphi = 0.3\%$, and $T_0 = 1100$ K. The correlation range and trap distribution are nearly identical to that of PFB. It was also found that both of these fits could be reproduced using an energetic landscape consisting of a trap distribution alone ($\varphi = 100\%$), with no Gaussian or correlated disorder. Excellent fits could be found at $T_0 = 450$ K and 560 K for PFB and F8BT, respectively, values very similar to those of Tanase *et al.*[8]

Constraints were applied to acceptable disorder parameter values, namely that these values must not just reproduce μ_0 and γ from Table II, but must also reproduce the PF relationship across the entire field range, with minimal deviation from the benchmark values of σ, to reduce the arbitrariness of these values. To test this further, simulations were run where the correlation was removed to see if the desired result could be reproduced using just some combination of the GDM with traps.

TABLE II. Parameters for PFB and F8BT polymer layers derived for zero carrier density.[23]

Parameter	PFB value	F8BT value
σ meV	110 ± 10	100 ± 10
μ_0 m^2/(Vs)	4×10^{-12}	2×10^{-12}
γ m$^{0.5}$ V$^{-0.5}$	6.4×10^{-4}	8.4×10^{-4}

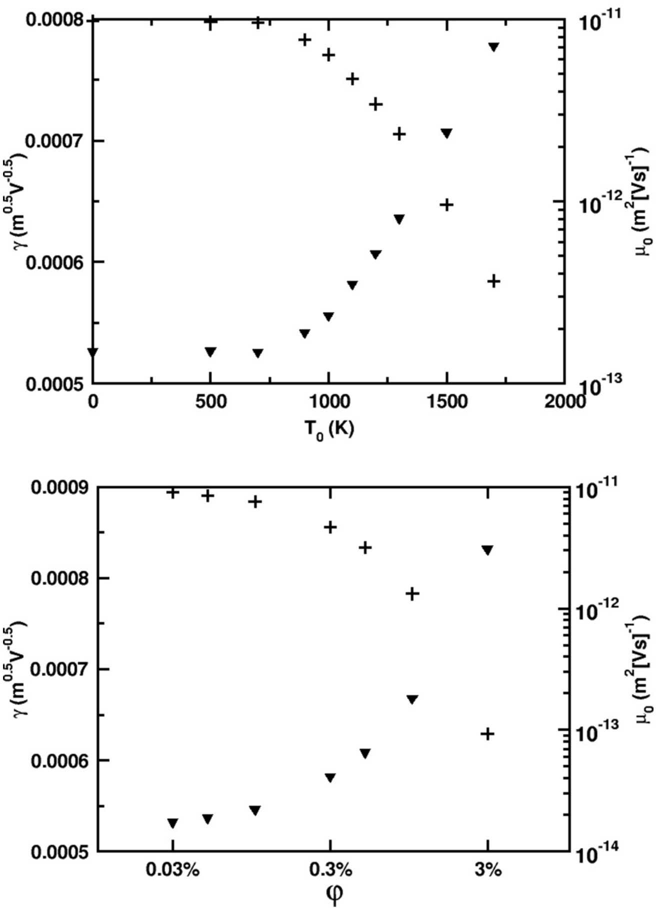

FIG. 5. Dependence of the zero-field mobility μ_0 (▼) and γ (+) on T_0 ($\varphi = 0.3\%$) and φ ($T_0 = 1100$ K).

It was found that this was not possible, that correlations must be included in order to recreate the mobility of PFB within the constraints given above. The results for F8BT clarify this, as it was not possible to create a close fit to the benchmark values while remaining within the σ range specified in Ref. 23. Although the μ_0 and γ could be reproduced for $\sigma = 100$ meV, PF dependence was not well reproduced down to low field. In other words, there are only a few parameter combinations that could fit the benchmark values within the constraints laid out above, and hence the values that were deduced are likely to give some real insight into the nature of the disorder present in the polymers under study.

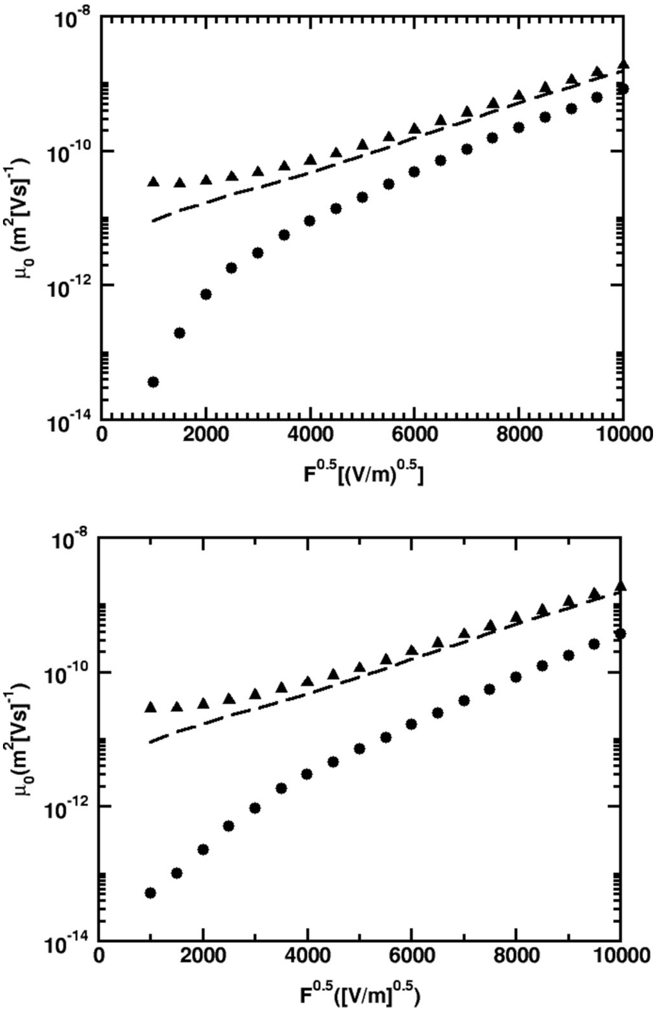

FIG. 6. Trap distribution dependence of mobility-field relationship. (φ,T_0) = (0.3%, 500 K) (▲), (0.3%, 1100 K) (dashed line), (0.3%, 1700 K) (●) in the top panel, and (0.03%, 1100 K) (▲), (0.3%, 1100 K) (dashed line), and (3%, 1100 K) (●).

Using the disorder parameters derived for single-particle mobility, J-V characteristics in single layers of PFB and F8BT devices have been investigated and the injection barriers derived. Figure 7 shows the results for a PFB hole-only device (HOD) at 295 K. The four sets of material parameters shown are those derived above. To reproduce the experimental current density in the presence of the high injection barrier, the hopping rate prefactor, ν_{hop}, used for the single-particle mobility, had to be raised by a factor of 10 so in this respect our parameter set is not fully transferable from the set used to obtain the single-particle mobility. The fourth (trap-only) distribution produces an excellent fit for $\phi_B = 0.47$ eV. In order to attain this fit, the hopping rate prefactor ν_{hop} had to be raised by almost three orders of magnitude. Figure 8 shows a comparison between experimental and KMC results for a 107-nm F8BT single-layer, electron-only device (EOD) at 297 K. As for the HOD, the large injection barrier forced an increase in the hopping rate prefactor ν_{hop}, used in the single-particle mobility, here by a factor of 10^3. No injection barrier could be found that would produce a fit for the equivalent trap-only distribution with $T_0 = 560$ K.

Our fitted injection barrier heights are higher than those implemented in the drift-diffusion model used in Ref. 23, where ohmic contacts and space-charge limited (SCL) behavior were assumed. However, later work has suggested that injection barriers may commonly exist in metal-organic interfaces that are normally assumed to be ohmic,[6] and other modeling work has reached the same conclusion.[52] This may account for the necessity of including injection barriers in the KMC model, especially as it includes an explicit hopping description between discrete energy levels, which is not included in drift-diffusion modeling.

The raising of the mobility prefactor, ν_{hop}, means that the same mobility has not been used in the present set of J-V

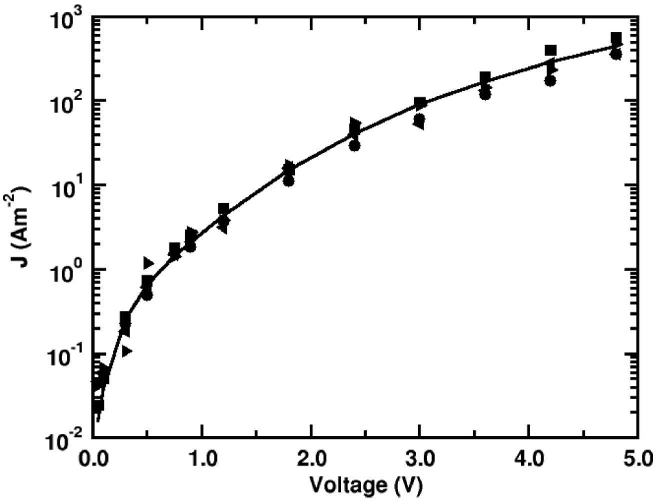

FIG. 7. Experiment (solid line) and KMC J-V characteristics for a PFB hole-only device (HOD). PFB layer width = 103 nm, $\sigma = 115$ meV, $\xi = 2$ nm, $\phi_B = 0.31$ eV, $(\varphi, T_0) = (0.1\%, 1600\text{ K})$ (◀), (0.3%, 1225 K) (■), (0.9%, 1050 K) (▶). Trap-only energetic landscape: $(\varphi, T_0) = (100\%, 450\text{ K})$, $\phi_B = 0.47$ eV (●).

simulations as was used in the single-particle mobility simulations. However, ν_{hop} just scales the mobility μ_0, it does nothing to the field dependence value, γ, which was reproduced by varying the material disorder. Therefore, scaling ν_{hop} cannot account for our reproduction of the voltage *dependence* of the current, only the overall magnitude. Further modeling, unpublished, revealed that a fit for the devices cannot be achieved for any other combination of ϕ_B, ν_{hop} and disorder description. A possible explanation for the requirement to increase ν_{hop} values is a change in polymer packing arrangements when contacts are added. The simulation of PV devices, below, provides an additional test of both the disorder description and the injection barriers derived.

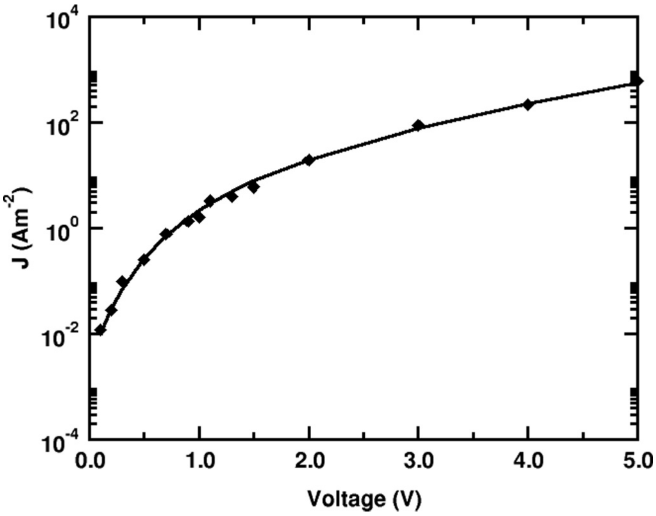

FIG. 8. Experiment (solid line) and KMC modeling (◆) results for an F8BT electron-only device (EOD), where 107 nm is the F8BT layer width, $\phi_B = 0.50$ eV $\sigma = 160$ meV, $\xi = 2$ nm, $(\varphi, T_0) = (0.3\%, 1100\text{ K})$.

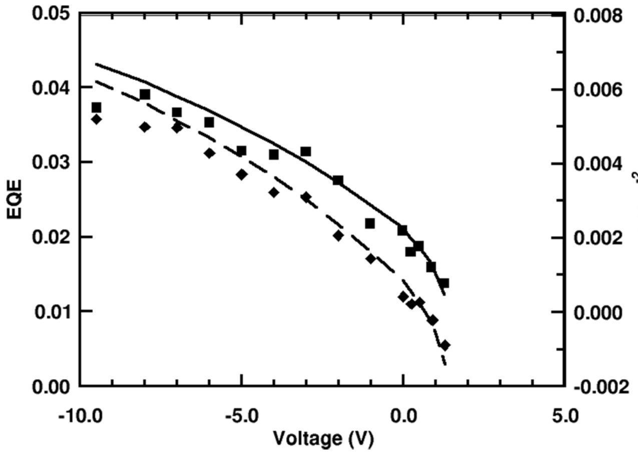

FIG. 9. Experimental EQE (dashed lines) and current density magnitude $|J|$ (solid lines) and KMC simulated EQE (◆) and J (■) for the bilayer device.

Figure 9 shows that an excellent fit to the experimental data for $|J|$ and the EQE in the bilayer device can be achieved for a recombination rate of $k_r = 1 \times 10^7\ \text{s}^{-1}$, the same value used by Groves *et al.*[32] for modeling geminate recombination in the same polymer combination, and similar to that measured by Westenhoff *et al.*[53] No parameters were adjusted from those that were derived from the previous work in this paper, that is, from the single-particle mobility and single layer device simulations. The bilayer device was not simulated in forward bias, as the origin of the measured current cannot be explained in our model given that both layers are unipolar. A possible origin is imperfections in the device structure or impurities in the polymers.

Figure 10 shows that the same value of k_r produces a reasonable fit, a factor of around 1.5 difference between the experimental and modeled data for $|J|$ and EQE in the blend device from −9.5 to 2.95 V. This agreement shows that not only is the photovoltaic regime being accurately modeled, but also that the injection description gives a good match at forward bias. The discrepancy is attributed to the uncertainty inherent

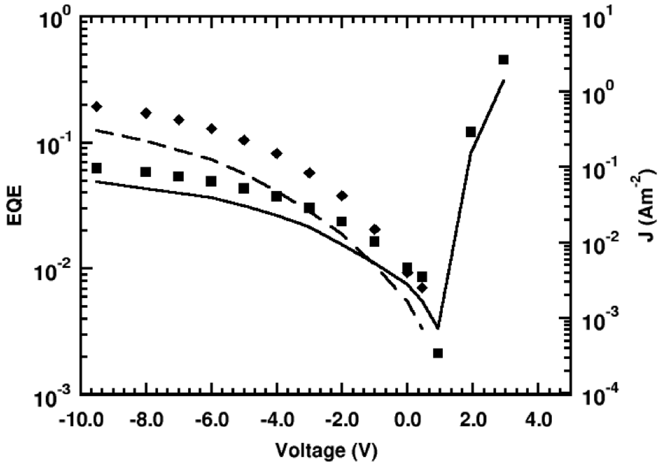

FIG. 10. As for Fig. 9 but here comparisons are made for the blend device. The inset shows the same data but here with $|J|$ plotted on a logarithmic scale and including forward bias.

to calculating the total amount of light absorbed in a polymer blend where limited information is available as to the internal domain size and structure and is small given the complexity of the system we are modeling. We stress that these results were produced without any adjustment of parameters to match the experimental data.

For adequate light absorption in OPVs, the thickness of material that can absorb light is 100 nm, since the polymer blend has an approximate light absorption coefficient from the data in Table I of $1 \times 10^5\ \mathrm{m}^{-1}$. The absorbed light generates excitons, which have to separate into free charges before they recombine. The photogenerated charges have to be extracted from the electrodes before they, in turn, recombine. The exciton diffusion length, the typical distance traveled before recombination, from Ref. 49 using the parameters for exciton hopping given in Sec. II, is around 4 nm.

To reduce the likelihood of exciton recombination, blends are used in which hole- and electron-conducting phases interpenetrate on a nanometer scale, creating a so-called bulk heterojunction. Most excitons can therefore reach an interface between the two phases before they recombine so η_{ed} is close to unity. However, the charges need to follow tortuous paths to reach the electrodes after creation by dissociation at an interface in which they are often close to the interface and so are likely to recombine. The predicted EQE in the simulation is very sensitive to the domain size. As noted in Sec. II, domain sizes cannot be measured but a typical domain size is less than 10 nm. At this stage in our effort to identify parameter values, feature size is the only remaining unknown we have already established everything else through building the model up, piece by piece. We found that 1.4 nm gave the best fit.

The much worse performance of the bilayer device compared to the blend device seen in Figs. 9 and 10 arises because the bilayer thicknesses, given in Table I, are many times the exciton diffusion length so the likelihood of exciton dissociation is greatly diminished, and the increase in η_{cc} due to the improved charge transport is not sufficient to compensate for the reduction in η_{ed}. As shown in Refs. 16 and 17, and seen in measurements of the power conversion efficiency on bulk heterojunction devices made from nanopatterned polymers,[54] there is an optimum interfacial area. We ran the simulation with a domain size of 2 nm, and the resulting EQE relationship increased, showing that our interfacial area is greater than the optimal value. One explanation for this result may be minority components in the blend domains that can have a measurable impact on the results since they act as dissociation, and hence recombination, centers. In a KMC model of PV blends, the interfacial area at which the peak in the internal quantum efficiency occurs, as determined by feature size, and the peak value are reduced by an amount that is sensitive to the percentage of minority component in the domains.[17]

IV. SUMMARY

We have developed a modeling procedure based on the KMC method that can account for the trap-filling effects commonly accounted for by a density-dependent factor in the mobilities.[26–29] KMC modeling provides insight into charge and energy transport in nanoscale landscapes. For instance, in drift-diffusion models, the PF relationship in Eq. (11) must be assumed, whereas in the KMC model, disorder descriptions that produce this relationship must first be found. Furthermore, the method used in this paper is highly applicable to complex, three-dimensional morphologies, which drift-diffusion modeling is unable to accurately represent. In addition to this, KMC modeling has the unique ability to incorporate factors that vary on the length scale of a carrier hop, such as the energetic disorder.

Alongside our previous work showing the unique capabilities of the KMC to assess the role of morphology and islands of impurities in determining device efficiency,[17] and, with others, for example, Refs. 12 and 55, giving insight into charge dissociation dynamics, here we find that the KMC is capable of providing insight into experimental measurements. We used dark J-V characteristics to validate our injection algorithm and deduce the injection barriers. By fitting the recombination rate to simulations with the parameter set obtained from the dark injection curve, we could reproduce the EQE and J-V characteristics of the devices under illumination, showing that not only can we reproduce the field dependency of the current, but also that the current magnitude is correct. This result goes a long way to validating our approach.

Successful reproduction of the experimental results for bilayer and blend devices at reverse and forward bias, without any adjustment of the material disorder parameters (derived from single-particle mobility modeling), or the injection barriers (derived from single layer devices), lends further credence to both the methodology and the values that have been derived in this work. As discussed above, the disorder parameter values influence not only the charge mobility, but also the exciton diffusion length, suggesting the exciton modeling is accurate as well. This goes a long way to validating each part of the method applied throughout this paper. Although only a limited range of forward bias voltage was modeled for the blend device, the close match to experiment lends some credence to the barrier heights derived for the unipolar devices.

Finally, our comparison between bilayer and blend devices bears out the link between device performance and interfacial area/domain size predicted by the KMC in Refs. 16 and 17 and recently seen experimentally by Park *et al.*[54] Successful simulation of charge injection and high current densities suggests that KMC is also capable of OLED simulation. Multiscale modeling would reduce the number of adjustable parameters still further, by deriving them using quantum chemical and molecular dynamics simulations.

ACKNOWLEDGMENTS

This work was supported by the European Commission FP-6 program MODE-COM (Grant No. NMP-CT-2006-016434) and the UK Engineering and Physical Sciences, EPSRC research grant Supergen Excitonic Cells Consortium. R.G.E.K. and E.N.W. thank the EPSRC for their studentships. Simulations were performed on the University of Bath High Performance Computing Cluster, *Aquila*.

[*] Present address: Department of Electronic and Electrical Engineering, University of Bath, Bath BA2 7AY, United Kingdom.

[†] a.b.walker@bath.ac.uk

[1] G. A. H. Wetzelaer, M. Kuik, M. Lenes, and P. W. M. Blom, Appl. Phys. Lett. **99**, 153506 (2011).

[2] G. A. H. Wetzelaer, L. J. A. Koster, and P. W. M. Blom, Phys. Rev. Lett. **107**, 066605 (2011).

[3] T. Kirchartz, B. E. Pieters, J. Kirkpatrick, U. Rau, and J. Nelson, Phys. Rev. B **83**, 115209 (2011).

[4] J. M. Montero and J. Bisquert, Solid-State Electron. **55**, 1 (2010).

[5] R. Steyrleuthner, S. Bange, and D. Neher, J. Appl. Phys. **105**, 064509 (2009).

[6] R. Steyrleuthner, M. Schubert, F. Jaiser, J. C. Blakesley, Z. Chen, A. Facchetti, and D. Neher, Adv. Mater. **22**, 2799 (2010).

[7] L. G. Kaake, P. F. Barbara, and X. Y. Zhu, J. Phys. Chem. Lett. **1**, 628 (2010).

[8] C. Tanase, E. J. Meijer, P. W. M. Blom, and D. M. de Leeuw, Phys. Rev. Lett. **91**, 216601 (2003).

[9] J. H. T. Williams and A. B. Walker, Nanotechnology **19**, 424011 (2008).

[10] G. A. Buxton and N. Clarke, Phys. Rev. B **74**, 085207 (2006).

[11] A. C. Morteani, P. Sreearunothai, L. M. Herz, R. H. Friend, and C. Silva, Phys. Rev. Lett. **92**, 247402 (2004).

[12] C. Groves, R. A. Marsh, and N. C. Greenham, J. Chem. Phys. **129**, 114903 (2008).

[13] J. J. M. vander Holst, M. A. Uijttewaal, B. Ramachandhran, R. Coehoorn, P. A. Bobbert, G. A. de Wijs, and R. A. de Groot, Phys. Rev. B **79**, 085203 (2009).

[14] L. J. A. Koster, Phys. Rev. B **81**, 205318 (2010).

[15] J. Nelson, J. J. Kwiatkowski, J. Kirkpatrick, and J. M. Frost, Acc. Chem. Res. **42**, 1768 (2009).

[16] P. K. Watkins, A. B. Walker, and G. L. B. Verschoor, Nano Lett. **5**, 1814 (2005).

[17] R. G. E. Kimber, A. B. Walker, G. E. Schröder-Turk, and D. J. Cleaver, Phys. Chem. Chem. Phys. **12**, 844 (2010).

[18] C. Groves, R. G. E. Kimber, and A. B. Walker, J. Chem. Phys. **133**, 144110 (2010).

[19] M. Casalegno, G. Raos, and R. Po, J. Chem. Phys. **132**, 094705 (2010).

[20] H. Yan, S. Swaraj, C. Wang, I. Hwang, N. C. Greenham, C. Groves, H. Ade, and C. R. McNeill, Adv. Funct. Mater. **20**, 4329 (2010).

[21] H. Bässler, Phys. Status Solidi B **175**, 15 (1993).

[22] U. Wolf, V. I. Arkhipov, and H. Bässler, Phys. Rev. B **59**, 7507 (1999).

[23] J. C. Blakesley, H. S. Clubb, and N. C. Greenham, Phys. Rev. B **81**, 045210 (2010).

[24] M. Jaiswal and R. Menon, Polym. Int. **55**, 1371 (2006).

[25] J. Zhou, Y. C. Zhou, J. M. Zhao, C. Q. Wu, X. M. Ding, and X. Y. Hou, Phys. Rev. B **75**, 153201 (2007).

[26] M. C. J. M. Vissenberg and M. Matters, Phys. Rev. B **57**, 12964 (1998).

[27] W. F. Pasveer, J. Cottaar, C. Tanase, R. Coehoorn, P. A. Bobbert, P. W. M. Blom, D. M. de Leeuw, and M. A. J. Michels, Phys. Rev. Lett. **94**, 206601 (2005).

[28] I. I. Fishchuk, D. Hertel, H. Bässler, and A. K. Kadashchuk, Phys. Rev. B **65**, 125201 (2002).

[29] M. Bouhassoune, S. L. M. Mensfoort, P. A. Bobbert, and R. Coehoorn, Org. El. **10**, 437 (2009).

[30] R. A. Marsh, C. Groves, and N. C. Greenham, J. Appl. Phys. **101**, 083509 (2007).

[31] I. Mitrani, *Simulation Techiques for Discrete Event Systems* (Cambridge University Press, Cambridge, 1982).

[32] C. Groves, J. C. Blakesley, and N. C. Greenham, Nano Lett. **10**, 1063 (2010).

[33] A. B. Walker, A. Kambili, and S. J. Martin, J. Phys.: Condens. Matter **14**, 9825 (2002).

[34] Y. N. Gartstein and E. M. Conwell, Chem. Phys. Lett. **245**, 351 (1995).

[35] F. C. Spano, J. Chem. Phys. **122**, 234701 (2005).

[36] F. C. Spano, S. C. J. Meskers, E. Hennebicq, and D. Beljonne, J. Am. Chem. Soc. **129**, 7044 (2007).

[37] F. Yang and S. R. Forrest, ACS Nano **2**, 1022 (2008).

[38] M. Casalegno, G. Raos, and R. Po, J. Chem. Phys. **132**, 094705 (2010).

[39] J. L. Brèdas, D. Beljonne, V. Coropceanu, and J. Cornil, Chem. Rev. **104**, 4971 (2004).

[40] V. Coropceanu, J. Cornil, D. A. da Silva Filho, Y. Olivier, R. Silbey, and J.-L. Brèdas, Chem. Rev. **107**, 926 (2007).

[41] R. W. Hockney and J. W. Eastwood, *Computer Simulation Using Particles* (Institute of Physics, Bristol, UK, 1992).

[42] S. Athanasopoulos, J. Kirkpatrick, D. Martinez, J. M. Frost, C. M. Foden, A. B. Walker, and J. Nelson, Nano Lett. **7**, 1785 (2007).

[43] A. J. Chatten, S. M. Tuladhar, S. A. Choulis, D. D. C. Bradley, and J. Nelson, J. Mater. Sci. **40**, 1393 (2005).

[44] A. Miller and E. Abrahams, Phys. Rev. **120**, 745 (1960).

[45] M. Scheidler, U. Lemmer, R. Kersting, S. Karg, W. Riess, B. Cleve, R. F. Mahrt, H. Kurz, H. Bässler, E. O. Gobel, and P. Thomas, Phys. Rev. B **54**, 5536 (1996).

[46] L. A. A. Pettersson, L. S. Roman, and O. Inganäs, J. Appl. Phys. **86**, 487 (1999).

[47] H. Hoppe, N. S. Sariciftci, and D. Meissner, Mol. Cryst. Liq. Cryst. **385**, 113 (2002).

[48] C. M. Ramsdale and N. C. Greenham, J. Phys. D **36**, 29 (2003).

[49] S. Athanasopoulos, E. V. Emelianova, A. B. Walker, and D. Beljonne, Phys. Rev. B **80**, 195209 (2009).

[50] S. V. Novikov, D. H. Dunlap, V. M. Kenkre, P. E. Parris, and A. V. Vannikov, Phys. Rev. Lett. **81**, 4472 (1998).

[51] R. G. E. Kimber, Ph.D. thesis, University of Bath, 2011.

[52] S. G. Stevenson, I. D. W. Samuel, S. V. Staton, K. A. Knights, P. L. Burn, J. H. T. Williams, and A. B. Walker, J. Phys. D **43**, 385106 (2010).

[53] S. Westenhoff, I. A. Howard, J. M. Hodgkiss, K. R. Kirov, H. A. Bronstein, C. K. Williams, N. C. Greenham, and R. H. Friend, J. Am. Chem. Soc. **130**, 13653 (2008).

[54] J. Park, N. Hendricks, and K. Carter, Langmuir **27**, 11251 (2011).

[55] C. Groves and N. C. Greenham, Phys. Rev. B **78**, 155205 (2008).